

Molecular Switching Operation in Gate Constricted Interface of MoS₂ and hBN Heterostructure

Rahul Tripathi¹, Pritam Bhattacharyya², Sukanta Nandi¹, Alok Shukla², Abha Misra^{1*}

¹Department of Instrumentation and Applied Physics, Indian Institute of Science, Bangalore, Karnataka, India 560012

²Department of Physics, Indian Institute of Technology Bombay, Powai, Mumbai, India 400076

Abstract

Combined diverse two-dimensional (2D) materials for semiconductor interfaces are attractive for electrically controllable carrier confinement to enable excellent electrostatic control. We investigated the transport characteristic in heterointerface of multilayer molybdenum disulfide and hexagonal boron nitride (MoS₂/h-BN) to reveal that the charge transfer switching (CTS) is highly dependent on both the local gate constriction and bias in the channel. Notably, the CTS is shown to be controlled at a molecular level through electro-tunable gated constriction. The resulting significant change in conductance due to exposing 100 parts-per-billion of nitrogen dioxide gas led to a high on/off ratio of 10² for completely switching off the channel thus, acting as a molecular switch. First-principle calculations further explained the mechanism of molecular CTS in the device. The molecular tunability of CTS has not been previously reported in any of the van der Waals semiconductor interfaces. Our finding opens avenues to exploit various atomically thin heterostructures for the mesoscopic transport phenomena towards molecular switching operation at room temperature.

Keywords: MoS₂, heterostructure, DFT, tunneling, molecular switch.

*Email: abha.misra1@gmail.com

INTRODUCTION

The electrically modulated switches are one of the most elementary components in electrical circuitry. Molecular-scale switches not only need miniaturization of the devices but also enable multifunctionalities, *e.g.*, robotics, memory, and neuromorphic computing, that are stable, reversible, writable, and addressable in solid-state devices.¹⁻⁴ So far, it has been challenging without the chemical process to achieve an efficient molecular switching by any external electrical field to switch the tunnel junction between two stable conductance states in the solid-state device.⁵⁻
⁷ Moreover, the reported molecular switches for memory applications with large on/off ratios (10^2 – 10^3) do not provide a non-volatile memory, thus cannot be used in applications that require all-electrically driven nanocircuit components.^{2,5-8} Therefore, there is a need for switching elements, which can be useful for the dual-functionality of electrical tunability and high on/off ratio. The *van der Waals* heterostructure (vdWHs) composed of two-dimensional (2D) materials are regarded as promising for the next generation nanodevices because of their unique band structure, enhanced features, and performance.^{9,10} The deterministic order of assembly with unprecedented control and accuracy to fabricate complex device architecture constitutes a remarkable paradigm to obtain unusual physical phenomena not observed in the pristine atomic layer.^{11,12} Importantly, controlling electron transport with gate-defined constriction allows electrical detection and manipulation of spin, charge, or valley degrees of freedom in these vdWHs.¹³⁻¹⁵ Among the family of 2D materials, transition metal dichalcogenides (TMDCs), represented by molybdenum disulfide (MoS_2), provide a promising platform due to their distinct electronic and chemical properties.¹⁶⁻¹⁹ In MoS_2 , the formation of tunneling barriers through nanostructures offers a unique perspective in terms of both carrier-confinement strength and the device geometry, which has been demonstrated recently in many experiments.^{15,20,21} Confining charge carriers in MoS_2 and forming one-dimensional

transport channel by electrostatic gating has been performed by Riccard et al.²¹ Lateral stacking of TMDCs offers the electrically controllable carrier confinement, combined with the diverse nature of 2D materials.^{14,20-28} The combination of different 2D materials into van der Waals heterostructures creates unprecedented physical phenomena, acting as a powerful tool for future devices. An exhaustive study of the band alignment and relativistic properties of a van der Waals heterostructure is done by Pierucci et al.²⁹ Furthermore, strong hybridization effects arising between the constitutive layers of a SnS₂/WSe₂ hetero-bilayer structure was studied by Zirbi et al.³⁰ The atomic flatness and lack of dangling at the surface of 2D insulators such as hexagonal boron nitride (h-BN) pave the way for a strongly coupled gate-defined quantum devices.³¹⁻³³ The ability to manipulate exciton dynamics by creating electrically reconfigurable confinement in MoS₂-WSe₂ vdWH led to an optical switch at room temperature.³⁴ Furthermore, such a local electrostatic gating enables a fine-tuning of the motion of electron near the channel with small external perturbation.¹⁵ Layer dependent study of MoS₂ transistors for molecular-sensing performances in the presence of gate bias and light irradiation is demonstrated by Late et al.³⁵ Furthermore, DFT calculations on single-layer and bilayer MoS₂ show that the dependence in the charge transfer process in the presence of an applied field. The MoS₂ field-effect transistor-based gas sensor has been widely studied because of the field-dependent nature of its electronic states, offering them optimal sensitivity by controlled gating of the sensors.³⁶⁻³⁹ The first principle calculation done by Yue et al. demonstrates that all molecules are physisorbed on monolayer MoS₂ with small charge transfer, acting as either charge acceptors or donors.³⁶ The application of a perpendicular electric field can also consistently modify the charge transfer between the adsorbed molecule and the MoS₂ substrate. A unique device architecture is designed by Sun et al. to induce tensile strain in bilayer graphene to prevent its mechanical deflection onto the substrate by

electrostatic force.³⁹ Furthermore, the adsorption rate can be controlled by the electric field introduced by applying a back-gate voltage. The significant change in conductance due to quantum confinement is observed earlier in a confined nanostructure in the proximity of an adsorbed molecule.^{40,41} In a report by Zhang et al., a large number of gates are employed for the enhanced electrostatic coupling between molecules and the active channel in a single-molecule transistor.^{20,42-44} Further, in another report, the combination of single-electron transistors with local gates provides a unique way of charge interaction with an external molecule observed in terms of quantum transport behavior of the system.^{45,46} However, electrical manipulation at room temperature is difficult due to the thermal excitation energy ($k_B T$) of the carriers. So far, precise carrier confinement is either enabled through the various arrangement of TMDC layers or controlling the carrier transport by a narrow gating to sense small perturbations. However, far less attention is given to understand the deterministic role of fine-tuned mutual independent gate architecture without applying a narrow pulse. Therefore, independent gates are essential for electrical field-dependent molecular interaction in the presence of external perturbation at room temperature operation.

We report a well-controlled charge transfer switching (CTS) upon molecular interaction in an archetypal vdWH based on a few-layer MoS₂ on top of the h-BN layer through electro-tunable gated constriction. A thin layer of h-BN is employed on pre-patterned electrodes with variable separations for a fine controlled potential barrier in the channel of MoS₂. It enables precise control of electron transport properties upon molecular interaction by independently controlling the bottom gates. The gate combination is essential to separately tune the position of the Fermi level and the carrier density in the channel. Furthermore, the combination of local gates allows defining an electron channel with an off-state when depleted. Transport characteristic revealed that the CTS

is a bias dependent conductance phenomenon in the channel due to the gating constriction. The channel conductance can be modulated up to three orders using source-drain bias. Furthermore, the gate combination allows a stepwise change in the conductance across the MoS₂ channel, which is observed for a fixed barrier width, and the magnitude is modulated using molecular interaction. Interestingly, the large-conductance change (10^2) due to 100 parts-per-billion (ppb) of gas concentration leads to a complete switching off the channel acting as a molecular switch. The electrical field-dependent tunability of CTS has not been previously reported in any atomically thin 2D materials. This observation opens avenues to utilize the variable gate architectural device to investigate mesoscopic transport phenomena for molecular interaction.

RESULTS

Devices were prepared by standard mechanical exfoliation of bulk MoS₂ and h-BN using the scotch tape technique, as shown schematically in Figure 1(a). A trilayer MoS₂ flake (~2 nm thick) is placed on top of a few-layer h-BN (~25 nm thick) flake using the standard dry transfer technique.⁴⁷ The bottom h-BN flake is thick enough to ensure an atomically flat surface and separates the MoS₂ layer from phonons and charge impurities present in the SiO₂ substrate. The flake thicknesses were first determined by the optical contrast and then confirmed by atomic force microscopy, as shown in Figure 1(b). The bottom h-BN works as a dielectric layer for local gates (V_{local}), whereas the global gate (V_{BG}) is provided with a p-Si/SiO₂ (~300 nm) substrate. The device consists of five gate electrodes as shown in Figure 1(c) acting as the local bottom gate with different widths are used to create a variable potential ladder varying from 50 to 1000 nm (W_{local}), enabling to evaluate of a systematic study on gate width-dependence on a single device (Figure S1). Figure 1(d) shows the Raman spectra of MoS₂ acquired at room temperature with a 532 nm excitation laser. The position of the E_{2g}^1 and A_{1g} modes agree well with the available literature on

Raman spectroscopy of thin MoS₂ flake. Both modes are sensitive to the number of atomic layers in the MoS₂ flake. The separation of E_{2g}^1 and A_{1g} peaks were measured to be 22.5 cm⁻¹, which confirms the trilayer MoS₂ flake.¹⁶ The carrier density in the MoS₂ channel is shown to be tuned by biasing the global gate (V_{BG}) as in Figure 1(e). Furthermore, a threshold voltage (V_{th}) around -12 V is observed with an on/off ratio of 10⁶, ensuring a well-tuned channel with V_{BG} . The carrier concentration in the pristine channel is estimated, $n_{MoS_2} = q^{-1}C_g|V_{th}| = 9.2 \times 10^{11} \text{ cm}^{-2}$ with $q = 9.2 \times 10^{-19} \text{ C}$ and $C_g = 1.23 \times 10^{-8} \text{ Fcm}^{-2}$ for 300 nm thick SiO₂ layer.

The output characteristic (source-drain current, I_{SD} versus source-drain voltage, V_{SD}) in Figure 2(a) is plotted with different V_{local} for the gate width of $W_{local} = 1000 \text{ nm}$ at room temperature. A dc voltage of 100 mV is applied across the channel results in a linear I - V characteristic indicating an Ohmic contact. For, $V_{local} = 0 \text{ V}$, the modulation of I_{SD} is observed with different V_{BG} from +20 to -20 V in a low bias regime, indicating a typical result for the n-doped device (Figure 2(b)). Furthermore, at positive V_{BG} , the conduction in the channel can be monotonically tuned by the local gate (1000 nm) at room temperature, down to a completely pinched off state which can be seen in Figure 2(c). The carrier concentration in the channel for the local gate is estimated as $n_{MoS_2}(local) = q^{-1}C_g|V_{th}| = 3.09 \times 10^{11} \text{ cm}^{-2}$ with $q = 9.2 \times 10^{-19} \text{ C}$ and $C_g = 1.41 \times 10^{-7} \text{ Fcm}^{-2}$ for 25 nm thick h-BN layer.

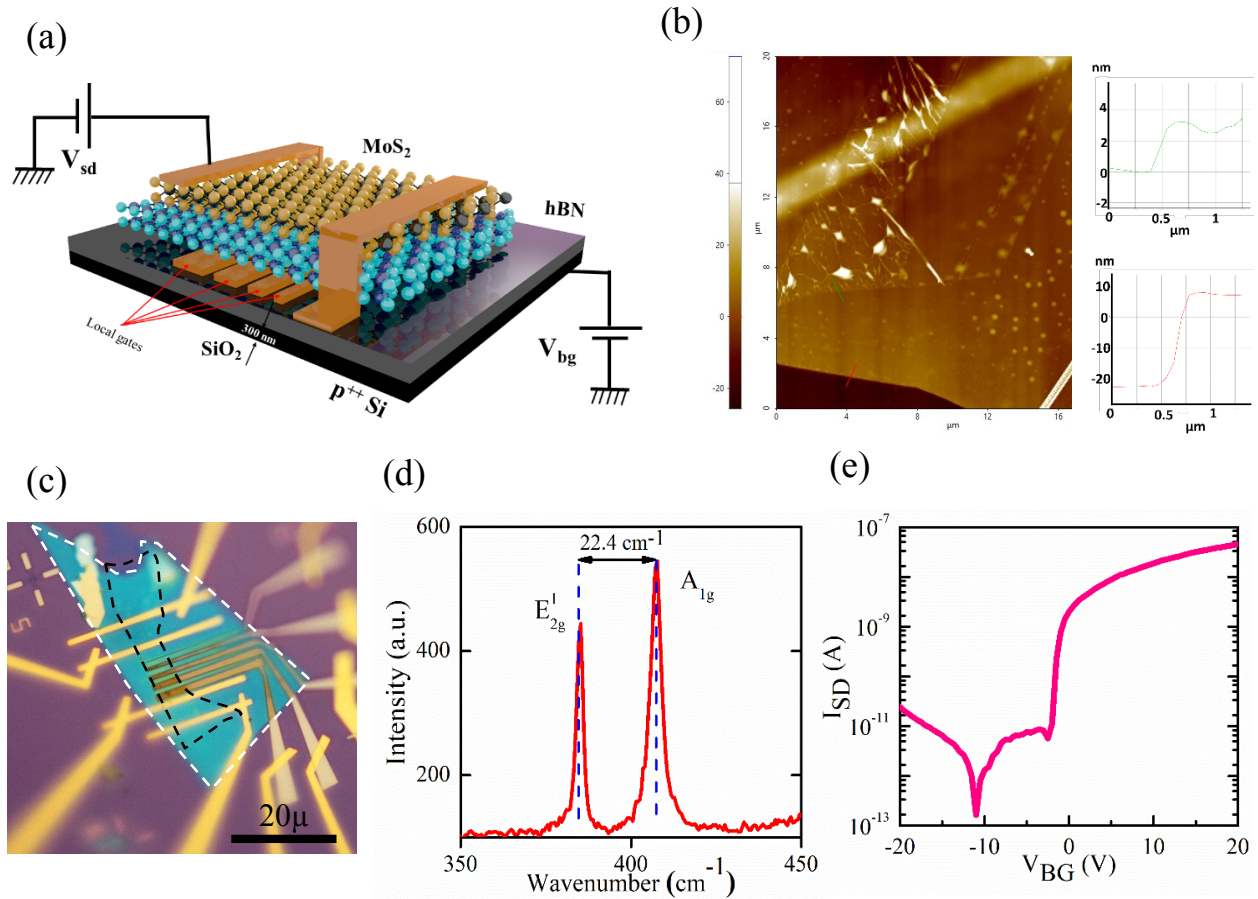


Figure 1. (a) Schematic of the device structure. (b) Microscopic optical image of the device. (c) Atomic force microscopy image of the MoS₂ and h-BN flakes. (d) Raman spectra of the MoS₂ flake. (e) Conductance measurement of the device with V_{BG} .

The variation in drain current using both the V_{BG} and V_{local} shows an interesting transition from ON state to OFF state for a fixed V_{SD} . To understand the phenomena, the difference in I_{SD} was carefully analyzed across the ON and OFF states of the device and extracted using $\Delta I_{SD} = (I_{(V_{local})} - I_{(V_{local})=-1V})$, as the current change is measured from the offset value ($V_{local} = -1$ V) to observe the change in conductance with switching effect. Furthermore, ΔI_{SD} is mapped as a function of V_{BG} and V_{local} (for a local gate of 1000 nm) (Figure 2(d)). The step-like feature is observed around -2 V of V_{local} , indicating a transition from a bulk metallic state to a bulk insulating state within the

depleted locally gated region. The flow of the electrons is highly influenced by the direct application of an electric field in the channel, which can be further evaluated using the source-drain bias.

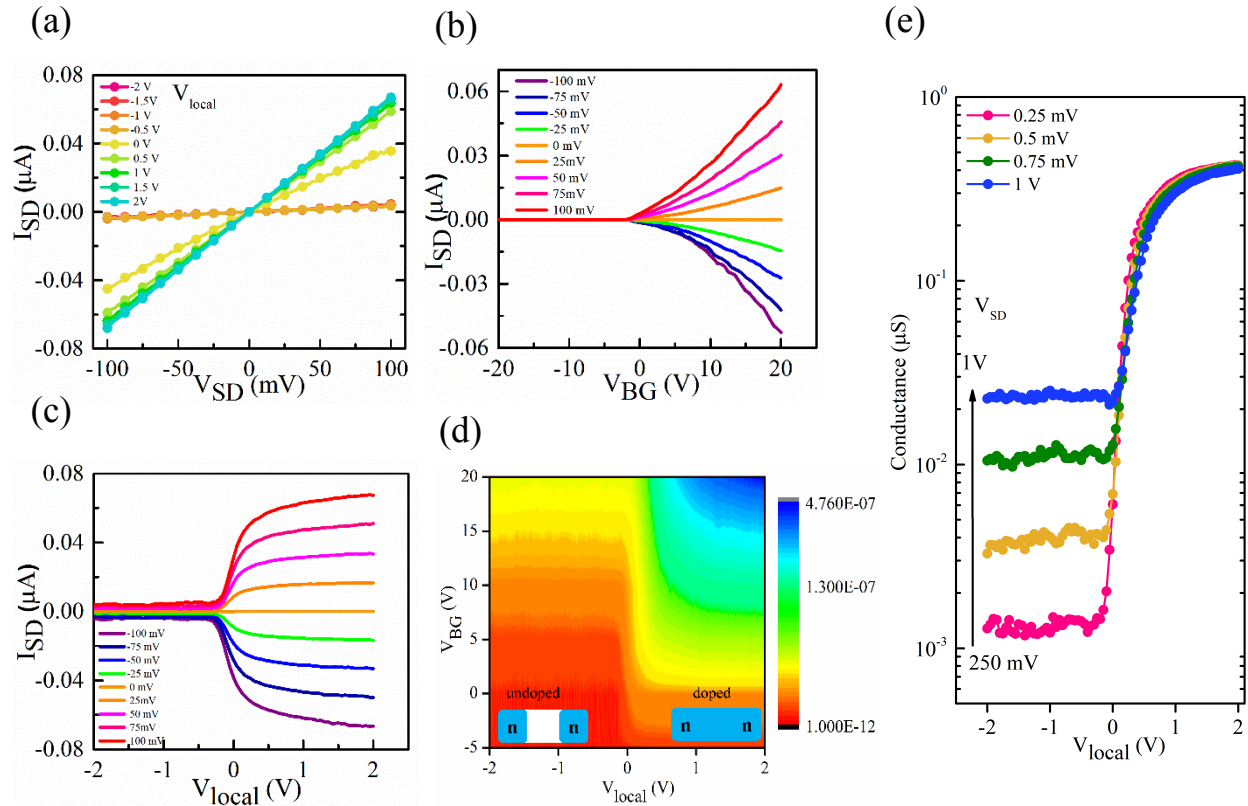


Figure 2. (a) I - V measurement of the device. (b) Variation in the drain current with global back-gate voltage. (c) Variation in the drain current with local gate voltage. (d) Color map of the drain current tuned by both V_{BG} and 1000 nm wide local gate, V_{local} at room temperature. (e) Conductance plot of the device tuned by different S - D bias at fixed $V_{BG}=+20$ V, at room temperature.

To eliminate the effect of extra carrier injection due to the applied bias, the conductance (G) of the channel is calculated for different V_{SD} . Interestingly, a stepwise movement of the conductance is observed in Figure 2(e), which was not observed in the doped region. The conductance of the channel can be tuned monotonically from 10^{-3} to $5 \times 10^{-1} \mu S$ by varying V_{SD} from 250 mV to 1 V.

The classical results presented in Figure 2(e) shows an abrupt termination of the charge transfer at the local gate voltage of $V_{local} = -2 V$, indicating the formation of a locally depleted region which is assumed insulating (Figure S2(a)). However, since the region is tunable by electrostatic field, electron tunneling may occur, which would make the channel conductive.⁴⁸ Therefore, a quantum mechanical model to account for the electron tunneling is required. Fundamentally, there are two types of tunneling: direct tunneling and Fowler-Nordheim (FN) tunneling.⁴⁹ Direct tunneling is significant for small gaps, while FN tunneling dominates if a high electric field is present in the gap. The characteristics of the potential barrier in the channel can further be evaluated with applied bias. Under small applied bias, the direct tunneling current through the barrier can be expressed as

$$I_{SD} \propto V_{SD} \exp\left(-\frac{2d\sqrt{2m^*\varphi}}{\hbar}\right)$$

where d , m^* and φ are the barrier thickness, effective electron mass and tunneling barrier height, \hbar is the reduced Planck constant. The contribution from direct tunneling current is negligibly small which can be seen in Figure 3(a). At higher source drain voltage, the potential barrier in the channel originates from the vertical electric field and the barrier becomes narrower, consequently leading to the Fowler-Nordheim (FN) tunneling.⁵⁰ The FN tunneling current is modeled by

$$I_{SD} \propto V_{SD}^2 \exp\left(-\frac{4d\sqrt{2m^*\varphi^3}}{3\hbar eV}\right)$$

From the above two equations, the plot of $\ln(I/V_{SD}^2)$ versus $1/V_{SD}$ should show a linear regime with a negative slope for the FN tunneling.

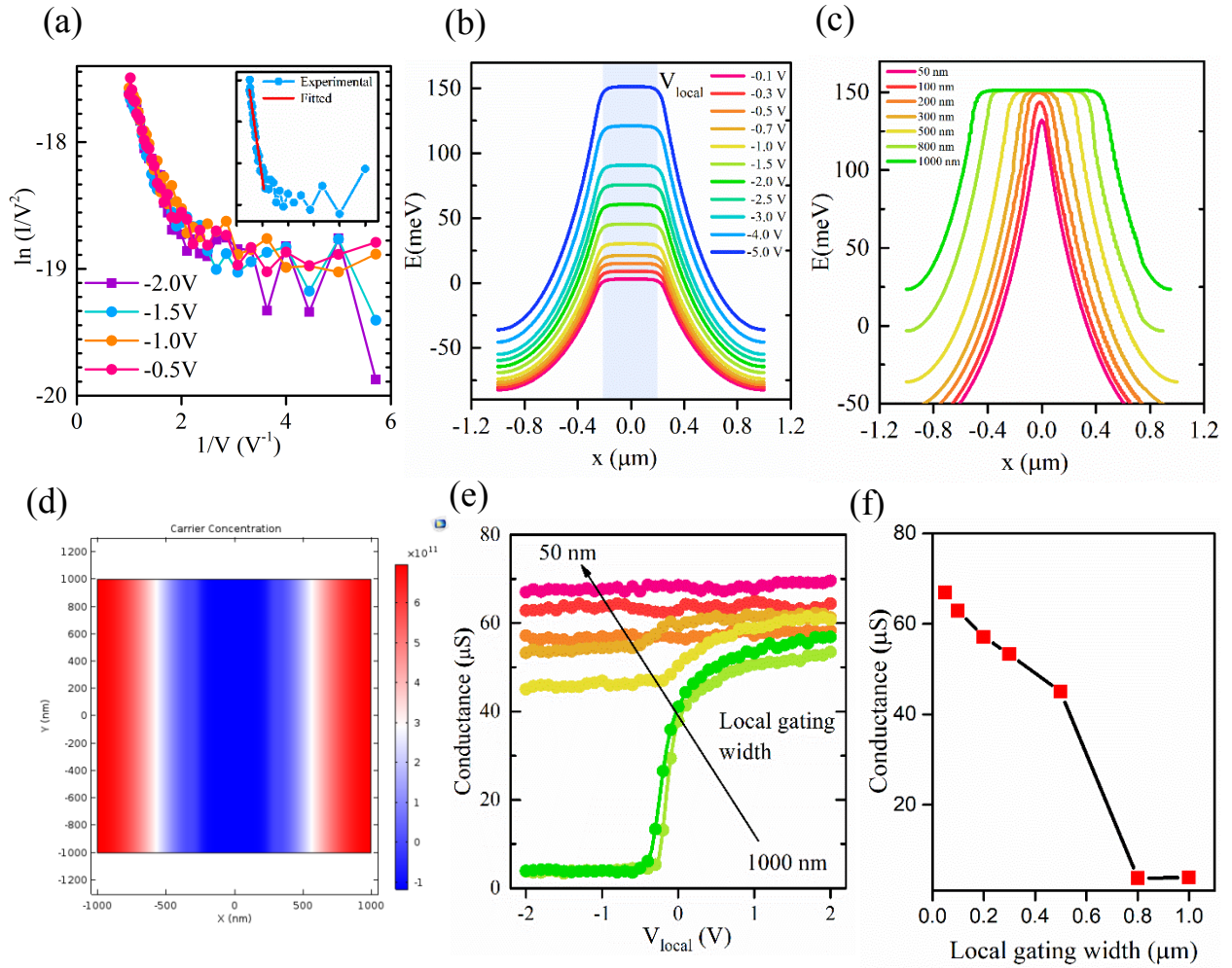


Figure 3. (a) Fowler-Nordheim plots for different local gate voltages for a fixed width of $W_{local} = 1000$ nm. (b) Simulated energy potential profile for different local gate voltages. (c) Simulated potential profile for different width (d) Self-consistent carrier density distribution for local gated geometry at $V_{BG} = +4$ V and $V_{local} = -1.5$ V. (e) Conductance plot of the device tuned by different widths of local gate (V_{local}) for a fixed S - D bias and $V_{BG} = +20$ V at room temperature. (f) CTS in the drain current with different widths at a fixed V_{SD} and $V_{local} = -1.5$ V.

The change in potential barrier height (ϕ) with the V_{local} can be extracted from the slope and threshold voltage in Figure 3(a). The threshold voltage for FN tunneling is calculated for all the V_{local} ($V_{local} = -2$ to -0.5 V) which turns out to be $1/2.49$ to $1/3.67$ V respectively, corresponding

to the barrier height (φ/e) of 0.401 to 0.240 eV in case of 1000 nm local gate width. Inset of Figure 3(a) shows the calculation for $V_{local} = -0.5 V$ where barrier is estimated to be about 0.24 eV from the slope, $\frac{4d\sqrt{2m^*\varphi^3}}{3he} = 1.02$ where $m^* = 0.5m_0$ is the effective mass of the electrons in MoS₂. The effective tunneling barrier width is also calculated from the inset of Figure 3(a), which is $d \approx 2.2$ nm. A self-consistent electrostatics simulation has been performed to calculate the potential barrier modulation with V_{local} across the channel. Figure 3(b) shows the modulation of the barrier height with different local gate voltages which is close to the value extracted from the fitting parameters. Interestingly, the vdWHs show a good contrast with conventional devices where the modulation in conductance is mostly obtained in the depletion region. This strongly implies that the vdWHs can be used as the tunneling device with a choice of appropriate local gate bias. The CTS *via* tunneling barrier can be tuned by two different voltages i.e. tunable barrier height by V_{local} and the type of tunneling by V_{SD} (Figure S2 (b, c)). For different widths of local gate, the tunneling barrier energy-space profile is shown in Figure 3(c). In the direct tunneling regime, when the external electric field is small, the tunneling barrier is dominated by the image charge potential. In this regime, the channel conductivity mainly depends on the width as shown in Figure 3(c). Carrier density modulation at the vicinity of the channel is extracted through the electrostatic simulation. The color mapping in Figure 3(d) represents a low charge carrier density near the local gated region at $V_{BG} = +4 V$ and $V_{local} = -1.5 V$, which is similar to the observed experimental data. To study the effect of the barrier width on the conductance, a series of different widths (W_{local}) of local gates were designed in a single channel with the same range of V_{local} . Figure 3(e) depicts the conductance as a function of V_{local} for different local gate widths varied from 50 to 1000 nm. For the wider channels ($W_{local} = 1000, 500$ nm), the conductance is fully controlled from an OFF-state to the ON-state, which can be explained in terms of depletion width. On the

other hand, Figure 3(d) depicts there is a stepwise movement in the conductance with lowering in W_{local} , which disappeared at $W_{local} = 50 \text{ nm}$, when there is no control over the channel (Figure S3). A temperature dependent study has been performed from 10 to 300 K at a fixed bias to observe the effect of temperature on the barrier (Figure S4). When the gap is small, electrons easily tunnel through the narrower barrier, the increased tunneling probability increases the tunneling electron density (channel conductivity).^{51,52} The calculated channel conductance is plotted as a function of width for a fixed V_{local} (Figure 3(f)). With the gap of 50 nm, the conductance value shows a value of $0.7 \times 10^2 \mu S$, large enough to support the channel conductance even at weak S - D electric fields. However, in this direct tunneling regime, the larger gap of 1000 nm does not support the charge transfer because the tunneling barrier width is too wide leading to a complete switching off the channel with a low conductance value of $\sim 6 \times 10^{-1} \mu S$ which is shown in Figure 3(f).

As discussed earlier, the CTS operation is mainly depending on the width of the local gates and the external electric field on the device, thus shows a potential for the molecular switching operation at room temperature. So far, a switching of the charge carriers is shown in the channel, which is further analyzed under external perturbation, in analogy with the source–drain bias of a conventional vdWHs. The effect of CTS on the molecular sensing ability of the device was evaluated using a controlled nitrogen dioxide (NO_2) gas environment. Initially, NO_2 gas is injected using mass flow controllers and the concentration of the gas is fixed for 100 ppb throughout the experiment. After 300 s, the injection was stopped. At a regular interval of time, a quick sweeping of local gate voltage was performed ($V_{local} = -2$ to $+2 \text{ V}$) at fixed V_{SD} and V_{BG} . Because of the nanometer-scale potential barrier width and the inversion layer located near the channel, the molecular interaction is seemingly distinct from other vdWHs. Figure 4(a) shows the response of the device with $W_{local} = 1000 \text{ nm}$ in the presence of gas molecules.

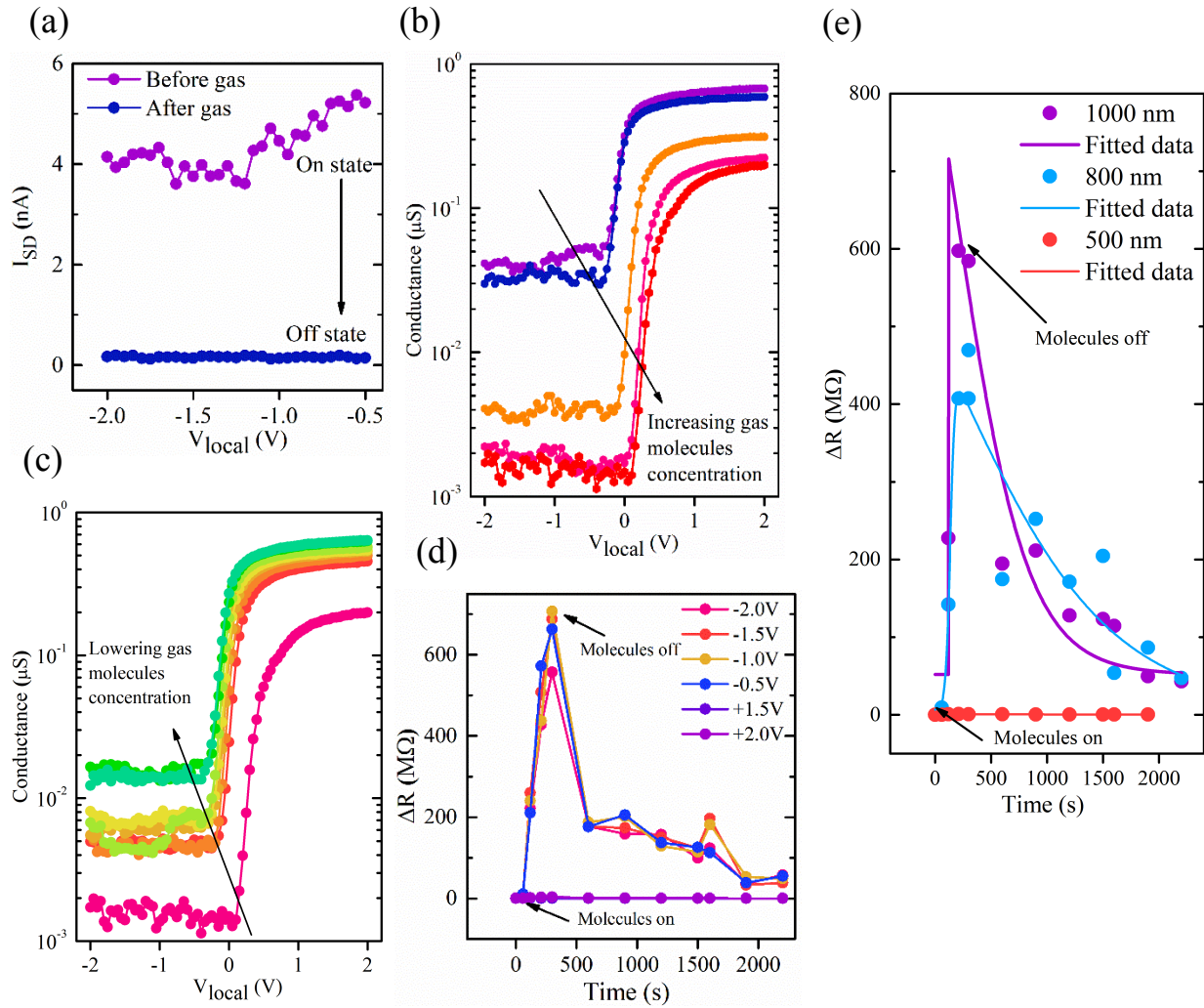


Figure 4. (a) Gate dependence of on/off state with the gas exposure. (b) Systematic change in the conductance with an increment in gas molecule concentration. (c) Switching of the channel from OFF to ON-state by lowering gas molecules concentration. (d) Change in resistance with gas exposure at different local gate voltage. (e) Molecular sensing response for different length of local gates with a non-linear fit of the experimental data.

The initial condition of the device was set to ON-state with a current value of $4.7 \times 10^{-9} A$, which turns to an OFF-state after gas exposure with $I_{SD} = 9 \times 10^{-11} A$. The concentration dependent study is performed by controlling the injection of molecules in the system for 300 s. A systematic

stepwise decrement in the conductance is observed with the increasing molecular concentration in the channel, which can be seen in Figure 4(b). There is almost a change of 10^2 in the conductance that occurs with the $V_{local} = -2$ to -0.5 V, where the barrier plays a crucial role in the charge conduction. A shift in the V_{th} is observed with the increasing molecular concentration indicating charge transfer mechanism in the vdWHs. Furthermore, the recovery of the device is also studied after the gas injection was stopped. Figure 4(c) depicts a stepwise increment in the conductance with lowering the gas molecule concentration. The change in resistance $[\Delta R = (R_{Without Gas} - R_{Gas})_{V_{local}=-1V}]$ was evaluated in Figure 4(d) with respect to time in presence /absence of molecules for different values of V_{local} . Interestingly, a clear dependence of flow of electron on the potential barrier under gas exposure is observed around $V_{local} = -2$ V, which is absent for the $V_{local} = +2$ V. There is a sharp increment in the resistance after the gas exposure that persists up to 300 s and decays slowly to its base value after switching off the gas injection. The peak value of the resistance is observed at around $V_{local} = -1$ V, which vanishes at positive gate bias of $V_{local} = +2$ V. Furthermore, the doping concentration in the channel can be plotted with time which is shown in Figure S5. The value of molecular adsorption rate can be extracted by fitting the curve to an equation $n_d(t) = \frac{n_0 p_a}{a} (\exp(-t/a) + n_a)$, where n_0 is the number of molecules injected in the system, n_a is the initial adsorption density in the MoS₂ and p_a is the adsorption rate. The extracted values of $n_0 p_a$ and $1/a$ are 7.20×10^{11} cm²/min and 0.104%/min, respectively, showing molecules adsorption density of 7.20×10^{11} cm²/min on MoS₂ and 0.104% of them desorbing in a minute. Consequently, the Fermi level of the system will further move towards valance band. Furthermore, the tunneling probability of electrons through the barrier will further reduce and the channel will behave as a complete insulator. The length dependence molecular sensing study using a series of local gates of different W_{local} is shown in Figure 4(e). The change in resistance (ΔR)

shows the length dependent sensing response with different W_{local} indicating an ON-to-OFF state transition after molecular interaction is more prominent with higher W_{local} . Figure 4(e) shows the fitting of the curve using an asymmetric double sigmoid function by an equation $\Delta R = \Delta R_0 + A * \left(\frac{1}{(1+\exp(-(t-B)))} \right) * \left(1 - \frac{1}{1+\exp(-(t-C))} \right)$, where A, B, C are the constants and ΔR_0 is the initial value of the resistance.

To understand the mechanism behind the CTS via tunneling, the quantum tunneling process is further analyzed under various scenarios. Figure 5 shows schematically how the CTS is critically affected in the presence of molecules which is also verified by density functional theory (DFT) calculations. The energy diagrams corresponding to the specific (hypothetical) case are drawn where the barrier height is shown without the applied bias and with the applied bias at the left contact and at $-2 V$ of V_{local} across the channel and no voltage drop at the right contact as shown in Figure 5(a) and 5(b). Enough bias is applied for a transition from a trapezoidal barrier to a triangular barrier as in Figure 5(b) and the position of the Fermi level can be tuned using the fixed V_{SD} ^{53,54} as well as by molecular interaction at a fixed V_{SD} . Further, the first-principle calculations were performed using DFT in NO₂ adsorbed monolayer MoS₂. We considered a 4×4 supercell of monolayer MoS₂ with one, two, and four NO₂ molecules within the supercell and the band structure of the single NO₂ adsorbed system is presented in Figure 5(c).

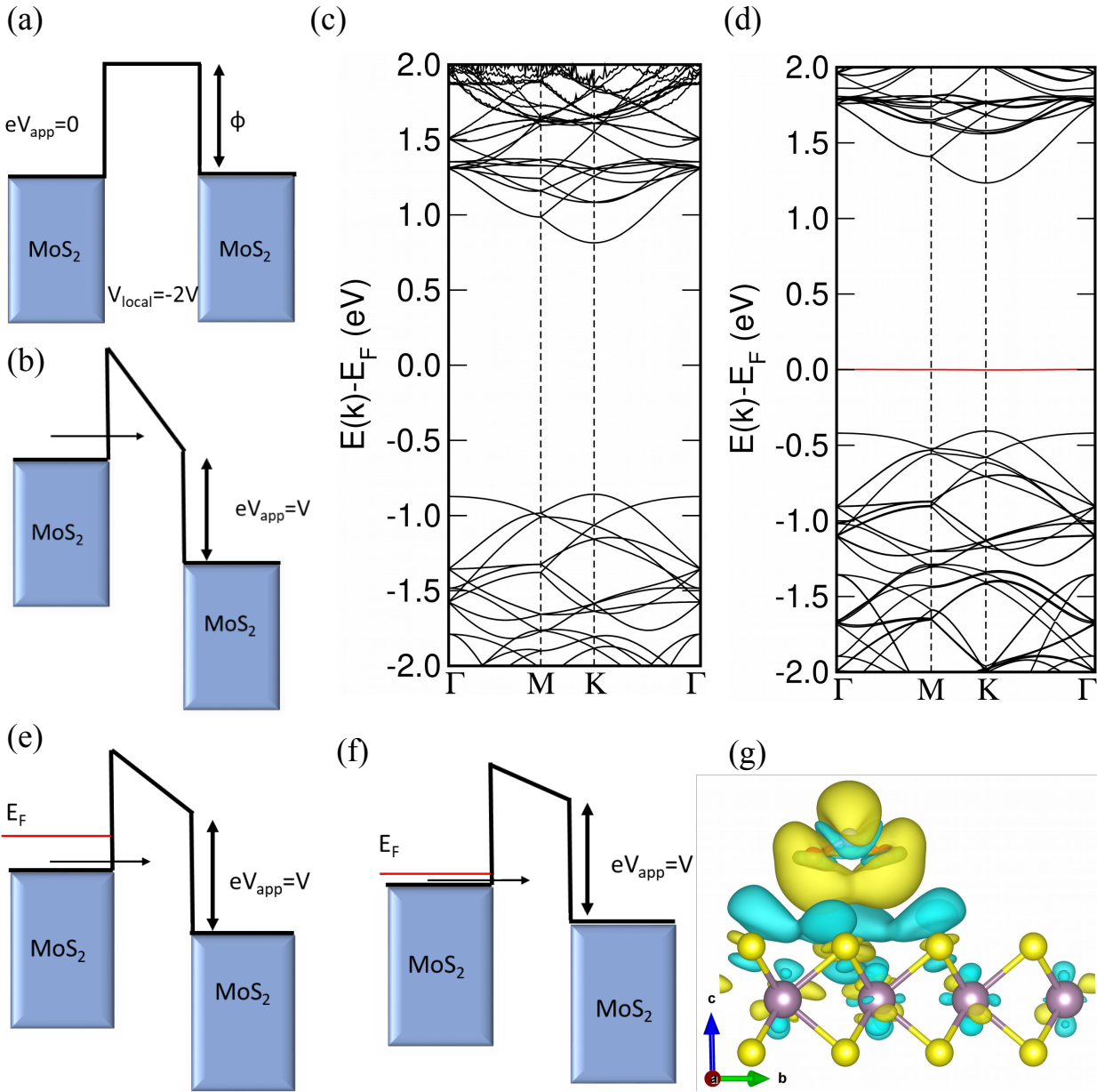


Figure 5. (a) Schematic energy diagram without and (b) with applied source-drain bias (V_{SD}). (c) Band structure of pristine MoS₂. (d) Change in the Fermi level position for single NO₂ molecule adsorbed in a 4×4 supercell of MoS₂. (e) Schematic of energy level shift after molecular exposure (f) with increasing molecular concentration. (g) Side-view of the differential charge density plot of the NO₂ adsorbed in a 4×4 supercell of monolayer MoS₂ system. The electron loss and rich regions are indicated by the cyan and yellow colors.

We observed that the red-colored band near the Fermi level derives predominant contributions from the NO₂ molecule. The band structures of the two and four NO₂ adsorbed systems are almost similar except for a shift of the Fermi level towards the valence band. Moreover, the number of energy levels between the valence and the conduction bands increases with the number of NO₂ molecules considered in the system. Figure 5(c) shows the band structure of monolayer MoS₂, which is in good agreement with the literature.⁵⁵ It is obvious from Figure 5(c) and 5(d) that in NO₂ adsorbed monolayer MoS₂ system, a significant shift of the Fermi level of 0.42 eV towards the valence band is observed as compared to the monolayer MoS₂.

The shift in Fermi level (ΔE_{Fermi}) with the increasing number of NO₂ molecules found out to be 0.50 and 0.57 eV for two and four NO₂ molecules, respectively. The effect of shift in Fermi level is shown schematically in Figure 5(e) and 5(f) where a transition from a triangular barrier to a trapezoidal barrier with a prominent CTS from ON-state to OFF-state. The differential charge density plots of a single NO₂ adsorbed monolayer MoS₂ system, depicted in Figure 5(g), confirms the electron transfer from monolayer MoS₂ surface to the adsorbed NO₂ molecule. The transferred charge are indicated by the cyan and yellow colors, respectively, with an isovalue of 1.98×10^{-4} e/Å³ from vdWHs to gas molecule and the effect of electron transfer, which also indicates the shifting of Fermi level towards the valence band. It is understood that the shift in the Fermi level increases with the concentration of NO₂ molecules, which also in accordance with our experimental study.

CONCLUSION

A novel approach to control the CTS in depletion region is demonstrated for the first time by engineering the dielectric environment. The multi-gate configuration is used to demonstrate an

electrically reconfigurable type of potential landscapes in a single channel. The charge transport through the tunable potential barrier using an in-plane electric field is governed by the carrier tunneling. A strong molecular induced modulation of doping effect is observed in MoS₂/h-BN vdWHs and a microscopic description of its origin is also discussed. The carrier movement (block or allow) in the vicinity of the channel with external perturbation is demonstrated, in analogy with source-drain bias of a conventional field effect transistor. Furthermore, the spatial confinement of the charge carriers due the potential barrier leads to an electrically controlled molecular switch using CTS mechanism. The formation of potential landscapes contributes to a new route to design and study quantum phenomena emerging from vdWHs for future study in molecular interactions.

MATERIALS AND METHODS

Device fabrication

Heterostructure of MoS₂ and graphene was fabricated with two different process for maximum molecular interaction. For the first process a two step lithography process was done on a clean Si/SiO₂ wafer without any flake to ensure the flatness and proper transfer of the flakes. In the first step the gate electrode was fabricated followed by deposition process of Cr/Au (5 nm/10 nm). A standard procedure of dry transfer technique using PDMS (Polydimethylsiloxane) stamp without using any sacrificial layer to ensure the good surface quality. A piece of glass was covered with a PDMS stamp (0.2-0.4 mm thick) which is transparent can be used under the microscope. Few layers of h-BN flake (HQ Graphene) were then exfoliated directly on the stamp and prepared for transfer on top of the local gate electrodes (For details see Supplementary information). Now, MoS₂ flake (varying up-to few layers) (Manchester Nanomaterial) was exfoliated onto the PDMS stamp and placed on the micromanipulator stage upside down and aligned perpendicularly with

the graphene flake using the microscope. The two were brought into contact and MoS₂ flake was transferred on top of h-BN. A 2nd layer of lithography process was done to form the contact pads with a deposition of Cr/Au (10 nm/70 nm).

Electrical and gas sensing measurements

Raman spectroscopy was performed in ambient condition, at a wavelength of 532 nm and with a light spot of 1 microns in different places of the device on MoS₂-h-BN heterostructure. The electrical characterization of the devices was carried out with an Agilent B1500A semiconductor analyzer in a closed chamber with a nitrogen environment after a stabilization process. Local gate dependent measurement was done by writing a script program for the dual sweep of gate voltage measurement port. Temperature dependent measurement was done in a high-vacuum chamber using Agilent B1500A semiconductor analyzer with a ramp of 25 °C. All the gas sensing experiments were performed at room temperature and atmospheric pressure. To achieve desirable concentration before being injected into the chamber the nitrogen di oxide gas was mixed with ultra-pure nitrogen gas. The concentration was fixed to 100 ppb of molecular concentration with a total flowrate of 1000 standard cubic centimeters per minute was maintained using the mass flow controllers throughout the experiment.

Theoretical Approach and Computational Details

The first principles calculations were performed using density functional theory⁵⁶ as implemented in the Vienna Ab-initio Simulation Package (VASP).^{57,58} All the calculations were carried out using projector-augmented wave (PAW) pseudo-potentials^{57,59} and Perdew-Burke-Ernzerhof (PBE) exchange correlation functional.⁶⁰ A kinetic energy cut-off of 500 eV and 5×5×1 k-mesh were considered for structural optimization. The threshold for energy and force convergence was

chosen to be 10^{-5} eV and 2×10^{-2} eV/Å, respectively, while with more than single NO₂ molecule in a 4×4 supercell, the force convergence criteria was set to be 5×10^{-2} eV/Å. The density of state calculations was carried out with a tighter threshold for energy convergence, i.e. 10^{-6} eV, and using a higher density of k-mesh, i.e. $21 \times 21 \times 1$. At least, a vacuum of 25 Å was considered along the z-direction to minimize the interactions with its images. We also incorporated the DFT-D2 method of Grimme^{61,62} to take into account the van der Waals force correction. To perform the band structure calculations, we employed 60 k-points in the reciprocal space. The differential charge density in single NO₂ adsorption can be defined as $\rho_{ad} = \rho_{\text{MoS}_2+\text{NO}_2} - \rho_{\text{MoS}_2} - \rho_{\text{NO}_2}$, where $\rho_{\text{MoS}_2+\text{NO}_2}$, ρ_{MoS_2} and ρ_{NO_2} are the charge densities of the monolayer MoS₂ + adsorbed NO₂, monolayer MoS₂, and isolated NO₂ molecule, respectively.

COMSOL simulation for potential barrier calculation

To complement and support our analysis of the barrier on the device, we carried out self-consistent electrostatic simulations of the carrier density in the MoS₂ plane as a function of the back-gate and local gate voltages. The geometry of the simulation is represented in Fig. S7. The dimensions of the different local gate width and the thicknesses of the SiO₂ and h-BN layers are close to those of the measured device. A sigmoid function was considered for simulation of the carrier density in MoS₂ sheet (For details see supplementary information). The Poisson's electrostatic static equation was solved with proper boundary conditions for different gate voltages. The profile of the potential energy ($E = -eV$ where e is the charge of the electron and V is the applied voltage at the local gate) across the local gated region is calculated for a fixed back-gate voltage and various local gate voltages and local gate widths.

REFERENCES

1. Jeong, H., Kim, D., Xiang, D. and Lee, T., 2017. High-yield functional molecular electronic devices. *ACS nano*, 11(7), pp.6511-6548.
2. Blum, A.S., Kushmerick, J.G., Long, D.P., Patterson, C.H., Yang, J.C., Henderson, J.C., Yao, Y., Tour, J.M., Shashidhar, R. and Ratna, B.R., 2005. Molecularly inherent voltage-controlled conductance switching. *Nature Materials*, 4(2), pp.167-172.
3. Cai, L., Cabassi, M.A., Yoon, H., Cabarcos, O.M., McGuinness, C.L., Flatt, A.K., Allara, D.L., Tour, J.M. and Mayer, T.S., 2005. Reversible bistable switching in nanoscale thiol-substituted oligoaniline molecular junctions. *Nano letters*, 5(12), pp.2365-2372.
4. Byun, J., Lee, Y., Yoon, J., Lee, B., Oh, E., Chung, S., Lee, T., Cho, K.J., Kim, J. and Hong, Y., 2018. Electronic skins for soft, compact, reversible assembly of wirelessly activated fully soft robots. *Science Robotics*, 3(18).
5. Kumar, S., Merelli, M., Danowski, W., Rudolf, P., Feringa, B.L. and Chiechi, R.C., 2019. Chemical locking in molecular tunneling junctions enables nonvolatile memory with large on-off ratios. *Advanced Materials*, 31(15), p.1807831.
6. van der Molen, S.J., Liao, J., Kudernac, T., Agustsson, J.S., Bernard, L., Calame, M., van Wees, B.J., Feringa, B.L. and Schönenberger, C., 2009. Light-controlled conductance switching of ordered metal- molecule- metal devices. *Nano letters*, 9(1), pp.76-80.
7. Schwarz, F., Kastlunger, G., Lissel, F., Egler-Lucas, C., Semenov, S.N., Venkatesan, K., Berke, H., Stadler, R. and Lörtscher, E., 2016. Field-induced conductance switching by charge-state alternation in organometallic single-molecule junctions. *Nature nanotechnology*, 11(2), pp.170-176.

8. Zhao, Y., Bertolazzi, S., Maglione, M.S., Rovira, C., Mas- Torrent, M. and Samorì, P., 2020. Molecular Approach to Electrochemically Switchable Monolayer MoS₂ Transistors. *Advanced Materials*, 32(19), p.2000740.
9. Novoselov, K.S., Mishchenko, A., Carvalho, A. and Neto, A.C., 2016. 2D materials and van der Waals heterostructures. *Science*, 353(6298).
10. Rozhkov, A.V., Sboychakov, A.O., Rakhmanov, A.L. and Nori, F., 2016. Electronic properties of graphene-based bilayer systems. *Physics Reports*, 648, pp.1-104.
11. Jariwala, D., Marks, T.J. and Hersam, M.C., 2017. Mixed-dimensional van der Waals heterostructures. *Nature materials*, 16(2), pp.170-181.
12. Liu, Y., Weiss, N.O., Duan, X., Cheng, H.C., Huang, Y. and Duan, X., 2016. Van der Waals heterostructures and devices. *Nature Reviews Materials*, 1(9), pp.1-17.
13. Goossens, A.S.M., Driessen, S.C., Baart, T.A., Watanabe, K., Taniguchi, T. and Vandersypen, L.M., 2012. Gate-defined confinement in bilayer graphene-hexagonal boron nitride hybrid devices. *Nano letters*, 12(9), pp.4656-4660.
14. Song, X.X., Liu, D., Mosallanejad, V., You, J., Han, T.Y., Chen, D.T., Li, H.O., Cao, G., Xiao, M., Guo, G.C. and Guo, G.P., 2015. A gate defined quantum dot on the two-dimensional transition metal dichalcogenide semiconductor WSe₂. *Nanoscale*, 7(40), pp.16867-16873.
15. Wang, K., De Greve, K., Jauregui, L.A., Sushko, A., High, A., Zhou, Y., Scuri, G., Taniguchi, T., Watanabe, K., Lukin, M.D. and Park, H., 2018. Electrical control of charged carriers and excitons in atomically thin materials. *Nature nanotechnology*, 13(2), pp.128-132.

16. Mak, K.F., Lee, C., Hone, J., Shan, J. and Heinz, T.F., 2010. Atomically thin MoS₂: a new direct-gap semiconductor. *Physical review letters*, 105(13), p.136805.
17. Cui, X., Lee, G.H., Kim, Y.D., Arefe, G., Huang, P.Y., Lee, C.H., Chenet, D.A., Zhang, X., Wang, L., Ye, F. and Pizzocchero, F., 2015. Multi-terminal transport measurements of MoS₂ using a van der Waals heterostructure device platform. *Nature nanotechnology*, 10(6), pp.534-540.
18. Pham, T., Li, G., Bekyarova, E., Itkis, M.E. and Mulchandani, A., 2019. MoS₂-based optoelectronic gas sensor with sub-parts-per-billion limit of NO₂ gas detection. *ACS nano*, 13(3), pp.3196-3205.
19. Late, D.J., Huang, Y.K., Liu, B., Acharya, J., Shirodkar, S.N., Luo, J., Yan, A., Charles, D., Waghmare, U.V., Dravid, V.P. and Rao, C.N.R., 2013. Sensing behavior of atomically thin-layered MoS₂ transistors. *ACS nano*, 7(6), pp.4879-4891.
20. Zhang, Z.Z., Song, X.X., Luo, G., Deng, G.W., Mosallanejad, V., Taniguchi, T., Watanabe, K., Li, H.O., Cao, G., Guo, G.C. and Nori, F., 2017. Electrotunable artificial molecules based on van der Waals heterostructures. *Science advances*, 3(10), p.e1701699.
21. Pisoni, R., Lei, Z., Back, P., Eich, M., Overweg, H., Lee, Y., Watanabe, K., Taniguchi, T., Ihn, T. and Ensslin, K., 2018. Gate-tunable quantum dot in a high quality single layer MoS₂ van der Waals heterostructure. *Applied Physics Letters*, 112(12), p.123101.
22. Epping, A., Banszerus, L., Güttinger, J., Krückeberg, L., Watanabe, K., Taniguchi, T., Hassler, F., Beschoten, B. and Stampfer, C., 2018. Quantum transport through MoS₂ constrictions defined by photodoping. *Journal of Physics: Condensed Matter*, 30(20), p.205001.

23. Lee, K., Kulkarni, G. and Zhong, Z., 2016. Coulomb blockade in monolayer MoS₂ single electron transistor. *Nanoscale*, 8(14), pp.7755-7760.
24. Thompson, J.J.P., Pei, D., Peng, H., Wang, H., Channa, N., Peng, H.L., Barinov, A., Schröter, N.B.M., Chen, Y. and Mucha-Kruczyński, M., 2020. Determination of interatomic coupling between two-dimensional crystals using angle-resolved photoemission spectroscopy. *Nature communications*, 11(1), pp.1-7.
25. Coy Diaz, H., Avila, J., Chen, C., Addou, R., Asensio, M.C. and Batzill, M., 2015. Direct observation of interlayer hybridization and Dirac relativistic carriers in graphene/MoS₂ van der Waals heterostructures. *Nano letters*, 15(2), pp.1135-1140.
26. Henck, H., Aziza, Z.B., Zill, O., Pierucci, D., Naylor, C.H., Silly, M.G., Gogneau, N., Oehler, F., Collin, S., Brault, J. and Sirotti, F., 2017. Interface dipole and band bending in the hybrid p– n heterojunction Mo S₂/GaN (0001). *Physical Review B*, 96(11), p.115312.
27. Zhang, K., Jariwala, B., Li, J., Briggs, N.C., Wang, B., Ruzmetov, D., Burke, R.A., Lerach, J.O., Ivanov, T.G., Haque, M. and Feenstra, R.M., 2018. Large scale 2D/3D hybrids based on gallium nitride and transition metal dichalcogenides. *Nanoscale*, 10(1), pp.336-341.
28. Zhang, Z., Qian, Q., Li, B. and Chen, K.J., 2018. Interface engineering of monolayer MoS₂/GaN hybrid heterostructure: modified band alignment for photocatalytic water splitting application by nitridation treatment. *ACS applied materials & interfaces*, 10(20), pp.17419-17426.
29. Pierucci, D., Henck, H., Avila, J., Balan, A., Naylor, C.H., Patriarche, G., Dappe, Y.J., Silly, M.G., Sirotti, F., Johnson, A.C. and Asensio, M.C., 2016. Band alignment and minigaps in monolayer MoS₂-graphene van der Waals heterostructures. *Nano letters*, 16(7), pp.4054-4061.

30. Zribi, J., Khalil, L., Zheng, B., Avila, J., Pierucci, D., Brulé, T., Chaste, J., Lhuillier, E., Asensio, M.C., Pan, A. and Ouerghi, A., 2019. Strong interlayer hybridization in the aligned SnS₂/WSe₂ hetero-bilayer structure. *npj 2D Materials and Applications*, 3(1), pp.1-7.
31. Lee, G.H., Cui, X., Kim, Y.D., Arefe, G., Zhang, X., Lee, C.H., Ye, F., Watanabe, K., Taniguchi, T., Kim, P. and Hone, J., 2015. Highly stable, dual-gated MoS₂ transistors encapsulated by hexagonal boron nitride with gate-controllable contact, resistance, and threshold voltage. *ACS nano*, 9(7), pp.7019-7026.
32. Cui, X., Lee, G.H., Kim, Y.D., Arefe, G., Huang, P.Y., Lee, C.H., Chenet, D.A., Zhang, X., Wang, L., Ye, F. and Pizzocchero, F., 2015. Multi-terminal transport measurements of MoS₂ using a van der Waals heterostructure device platform. *Nature nanotechnology*, 10(6), pp.534-540.
33. Xue, J., Sanchez-Yamagishi, J., Bulmash, D., Jacquod, P., Deshpande, A., Watanabe, K., Taniguchi, T., Jarillo-Herrero, P. and LeRoy, B.J., 2011. Scanning tunnelling microscopy and spectroscopy of ultra-flat graphene on hexagonal boron nitride. *Nature materials*, 10(4), pp.282-285.
34. Unuchek, D., Ciarrocchi, A., Avsar, A., Watanabe, K., Taniguchi, T. and Kis, A., 2018. Room-temperature electrical control of exciton flux in a van der Waals heterostructure. *Nature*, 560(7718), pp.340-344.
35. Late, D.J., Huang, Y.K., Liu, B., Acharya, J., Shirodkar, S.N., Luo, J., Yan, A., Charles, D., Waghmare, U.V., Dravid, V.P. and Rao, C.N.R., 2013. Sensing behavior of atomically thin-layered MoS₂ transistors. *ACS nano*, 7(6), pp.4879-4891.

36. Yue, Q., Shao, Z., Chang, S. and Li, J., 2013. Adsorption of gas molecules on monolayer MoS₂ and effect of applied electric field. *Nanoscale research letters*, 8(1), p.425.
37. Ao, Z.M., Li, S. and Jiang, Q., 2010. Correlation of the applied electrical field and CO adsorption/desorption behavior on Al-doped graphene. *Solid State Communications*, 150, pp.680-683.
38. Zhu, X.F., Wang, L. and Chen, L.F., 2014. Adsorption and dissociation of O₂ on MoSe₂ and MoTe₂ monolayers: ab initio study. *International Journal of Modern Physics B*, 28(28), p.1450195.
39. Sun, J., Muruganathan, M. and Mizuta, H., 2016. Room temperature detection of individual molecular physisorption using suspended bilayer graphene. *Science advances*, 2(4), p.e1501518.
40. Stokbro, K., 2010. First-principles modeling of molecular single-electron transistors. *The Journal of Physical Chemistry C*, 114(48), pp.20461-20465.
41. Kubatkin, S., Danilov, A., Hjort, M., Cornil, J., Bredas, J.L., Stuhr-Hansen, N., Hedegård, P. and Bjørnholm, T., 2003. Single-electron transistor of a single organic molecule with access to several redox states. *Nature*, 425(6959), pp.698-701.
42. Wu, S., Fatemi, V., Gibson, Q.D., Watanabe, K., Taniguchi, T., Cava, R.J. and Jarillo-Herrero, P., 2018. Observation of the quantum spin Hall effect up to 100 kelvin in a monolayer crystal. *Science*, 359(6371), pp.76-79.
43. Wold, D.J. and Frisbie, C.D., 2001. Fabrication and characterization of metal– molecule– metal junctions by conducting probe atomic force microscopy. *Journal of the American Chemical Society*, 123(23), pp.5549-5556.

44. Jia, C., Grace, I.M., Wang, P., Almeshal, A., Huang, Z., Wang, Y., Chen, P., Wang, L., Zhou, J., Feng, Z. and Zhao, Z., 2020. Redox Control of Charge Transport in Vertical Ferrocene Molecular Tunnel Junctions. *Chem.*
45. Ray, S.J., 2016. First-principles study of MoS₂, phosphorene and graphene based single electron transistor for gas sensing applications. *Sensors and Actuators B: Chemical*, 222, pp.492-498.
46. Famili, M., Jia, C., Liu, X., Wang, P., Grace, I.M., Guo, J., Liu, Y., Feng, Z., Wang, Y., Zhao, Z. and Decurtins, S., 2019. Self-assembled molecular-electronic films controlled by room temperature quantum interference. *Chem*, 5(2), pp.474-484.
47. Wang, J.I.J., Yang, Y., Chen, Y.A., Watanabe, K., Taniguchi, T., Churchill, H.O. and Jarillo-Herrero, P., 2015. Electronic transport of encapsulated graphene and WSe₂ devices fabricated by pick-up of prepatterned hBN. *Nano letters*, 15(3), pp.1898-1903.
48. Barbour, J.P., Dolan, W.W., Trolan, J.K., Martin, E.E. and Dyke, W.P., 1953. Space-charge effects in field emission. *Physical Review*, 92(1), p.45.
49. Fowler, R.H. and Nordheim, L., 1928. Electron emission in intense electric fields. *Proceedings of the Royal Society of London. Series A, Containing Papers of a Mathematical and Physical Character*, 119(781), pp.173-181.
50. Ikuno, T., Okamoto, H., Sugiyama, Y., Nakano, H., Yamada, F. and Kamiya, I., 2011. Electron transport properties of Si nanosheets: Transition from direct tunneling to Fowler-Nordheim tunneling. *Applied Physics Letters*, 99(2), p.023107.
51. Wu, L., Duan, H., Bai, P., Bosman, M., Yang, J.K. and Li, E., 2013. Fowler–Nordheim tunneling induced charge transfer plasmons between nearly touching nanoparticles. *ACS nano*, 7(1), pp.707-716.

52. Doan, M.H., Jin, Y., Adhikari, S., Lee, S., Zhao, J., Lim, S.C. and Lee, Y.H., 2017. Charge transport in MoS₂/WSe₂ van der Waals heterostructure with tunable inversion layer. ACS nano, 11(4), pp.3832-3840.
53. Simmons, J.G., 1963. Generalized formula for the electric tunnel effect between similar electrodes separated by a thin insulating film. Journal of applied physics, 34(6), pp.1793-1803.
54. Lu, J.G., 2004. Single electronics. In Introduction to Nanoscale Science and Technology (pp. 261-312). Springer, Boston, MA.
55. Kan, M., Wang, J.Y., Li, X.W., Zhang, S.H., Li, Y.W., Kawazoe, Y., Sun, Q. and Jena, P., 2014. Structures and phase transition of a MoS₂ monolayer. The Journal of Physical Chemistry C, 118(3), pp.1515-1522.
56. Kohn, W. and Sham, L.J., 1965. Self-consistent equations including exchange and correlation effects. Physical review, 140(4A), p.A1133.
57. Kresse, G. and Furthmüller, J., 1996. Efficient iterative schemes for ab initio total-energy calculations using a plane-wave basis set. Physical review B, 54(16), p.11169.
58. Kresse, G. and Furthmüller, J., 1996. Efficiency of ab-initio total energy calculations for metals and semiconductors using a plane-wave basis set. Computational materials science, 6(1), pp.15-50.
59. Blöchl, P.E., 1994. Projector augmented-wave method. Physical review B, 50(24), p.17953.
60. Perdew, J.P., Burke, K. and Ernzerhof, M., 1996. Generalized gradient approximation made simple. Physical review letters, 77(18), p.3865.

61. Grimme, S., 2006. Semiempirical GGA- type density functional constructed with a long-range dispersion correction. *Journal of computational chemistry*, 27(15), pp.1787-1799.
62. Kan, M., Wang, J.Y., Li, X.W., Zhang, S.H., Li, Y.W., Kawazoe, Y., Sun, Q. and Jena, P., 2014. Structures and phase transition of a MoS₂ monolayer. *The Journal of Physical Chemistry C*, 118(3), pp.1515-1522.